ELSEVIER

Thermochimica Acta 388 (2002) 183–197

thermochimica
acta

www.elsevier.com/locate/tca

Measurement and modeling of individual carbonaceous particle temperature profiles during fast CO_2 laser heating
Part 1. Model char

Ashish Tripathi[a], Chris L. Vaughn[a], Waleed Maswadeh[b],
Henk L.C. Meuzelaar[a,*]

[a]*Center for Microanalysis and Reaction Chemistry, The University of Utah, Salt Lake City, UT 84112, USA*
[b]*Geo-Centers, E3220 Aberdeen Proving Grounds, Aberdeen, MD 21010, USA*

Received 28 June 2001; received in revised form 4 October 2001; accepted 4 October 2001

Abstract

To investigate the chemical kinetics of coal pyrolysis under pulverized coal combustion conditions (coal particles of up to 100 μm diameter heated in excess of 10^5 K/s to 1500–2000 K), it is imperative to characterize the time–temperature profile and intraparticle temperature gradients during the heating phase. A CO_2 laser pyrolysis system with two-color micropyrometry system was developed to heat single particles in the 50–120 μm range to 1400–1800 K in 50 ms and measure the time–temperature profile. Before attempting to investigate coal particles, inert spherical carbonaceous particles (i.e. Spherocarb) were selected to investigate system performance and reliability. Part 1 of the article details the experiments on Spherocarb.

Spherocarb particles of 80, 100 and 120 μm diameter, respectively, were irradiated with 10.6 μm wavelength, 30 ms duration CO_2 laser pulses, at two different intensity levels and their temperature histories were measured with a specially built two-color micropyrometry system. A heat transport model was used to predict the particle surface temperature histories. The density of the porous Spherocarb particles (one value used for all the cases), as well as the total laser flux absorbed, were used as fitting parameters, thus allowing numerical extraction of absorbed laser power values as a function of particle size. These parameters can be used to model the temperature histories of similar size coal particles. Moreover, this analysis can also help to evaluate the reliability of the two-color micropyrometer system. Based upon the modeling results an estimation of intraparticle temperature gradients were made.

Keywords: Laser pyrolysis; Pulverized coal combustion; Heat transfer modeling

1. Introduction

To understand the devolatilization kinetics of rapidly heated coal particles, recording accurate temperature histories is one of the most important prerequisites. Furthermore, measurement and/or estimation of the inherent intraparticle temperature gradients are required in order to use the measured surface temperature data. Before attempting to acquire and analyze temperature histories of highly complex reacting substances, such as coal particles, we selected a simple, non-devolatilizing, well-characterized carbonaceous particle, namely Spherocarb (Analabs), as a model system. The high heating rates observed under pulverized

---

[*] Corresponding author.
E-mail address: meuzelaar@mail.marc.utah.edu
(H.L.C. Meuzelaar).

PII: S0040-6031(02)00029-1

coal combustion are achieved by a CO_2 laser heating system described elsewhere [1]. The particle surface temperature history is measured by an in-house built two-color micropyrometry system [2]. A heat transport model is used to model the particle surface temperature history and to estimate the intraparticle temperature gradients. This enables a better understanding of the performance of the specially constructed CO_2 laser heating system and two-color micropyrometer.

Spherocarb particles are spherical in shape and are available in a 70–120 μm diameter range. The physical properties of these particles are consistent (the manufacturer suggests typical standard deviations to be <10%). Not only are these particles stable at relatively high temperatures, but also their heating behavior has been studied extensively [3–8].

Following the basic approach described by Maloney and co-workers [5–7] and others [3,9–13], a simple energy balance heat transport model was written to verify the heating behavior of the Spherocarb particles, as well as to characterize the performance of our CO_2 laser heating system and dual wavelength micropyrometer.

2. Experimental

2.1. CO_2 laser and optics

The CO_2 laser (Apollo, model 3050 OEM) is electronically triggered to produce a pulse of precise duration. The 8 mm diameter laser beam is 47.5% reflected and 52.5% transmitted by a beam splitter. Both the reflected and transmitted beams are individually focused at the center of the cell using high power mirror objectives (Spawr Corporation, model FM90). The optical configuration is displayed in Fig. 1. Based on the luminous laser beam footprints on quartz wafers [2], the laser beam waist can be estimated to be approximately 350 μm in diameter with delivered laser energy fluxes in the 4–80 MW/m^2 range. Two low power HeNe laser beams (Uniphase, model 1508-0, output 0.95 mW) are positioned to be co-axial and co-focal with the CO_2 laser beams. This facilitates visual positioning of the particle at the point of intersection of the two laser beams. The energy output of the CO_2 laser beam pulse is measured using an integrating beam energy meter (Scientech AC50HD), which receives about 10% of the emitted laser power radiation.

2.2. Two-color radiation pyrometer

To measure the surface temperature history of the laser heated particle; a two-color radiation micropyrometry subsystem was constructed. The construction, theory, choice of wavelengths and computational techniques used are described in detail by Maswadeh and co-workers [2,13]. Fig. 2 presents the schematic layout of the two-color pyrometer. Emitted radiation from the heated particle is concentrated by a Cassegrainian-type reflective objective (Ealing Optics 15/.28×) and mechanically chopped at a chopping frequency up to 3 kHz (Stanford Research Systems, model SR540). The chopped radiation beam is split by a 5.065–5.364 μm wavelength bandpass filter (Optical Filter Corporation). This filter transmits 5.065–5.364 μm wavelength radiation, which is focused on a liquid nitrogen-cooled InSb IR detector

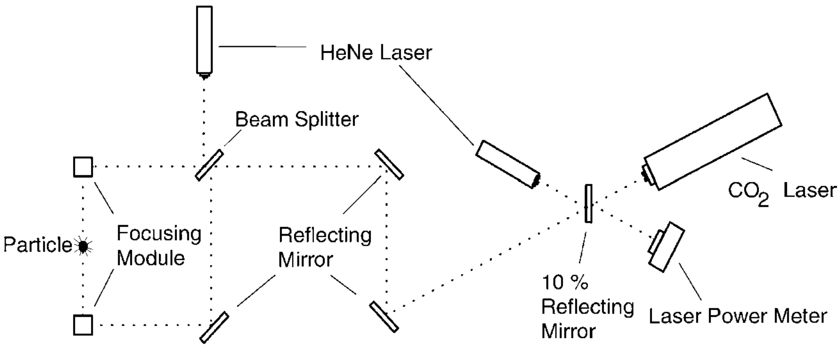

Fig. 1. Top view of the laser focusing arrangement.

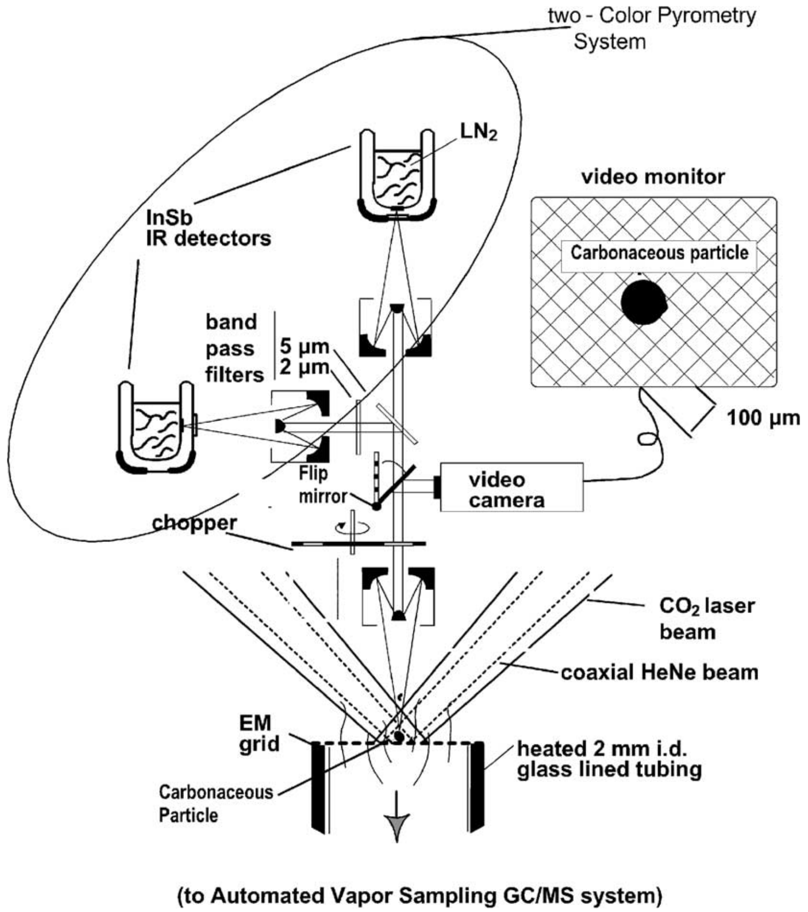

Fig. 2. Schematic setup of the two-color micropyrometer, the video microscope and laser pyrolysis stage.

(Barnes Engineering, model DO4EJ) using a second Cassegrainian-type reflective objective. The remaining radiation is reflected, filtered through a 1.811–2.11 μm wavelength bandpass filter (Optical Filter Corporation) and focused on a second liquid nitrogen-cooled InSb IR detector (Barnes Engineering, model DO4EJ) using a third Cassegrainian-type reflective objective. The two Dewar-mounted, liquid nitrogen-cooled IR detectors send their output to a pair of home-built, low-noise current amplifiers (amplification factor approximately 10^6). The amplified signal is acquired by a MS DOS based desktop computer via a high speed, 16 bit resolution A/D conversion board (HSDAS-16, Analogic Inc.) capable of acquiring data at 200 kHz, with the help of SnapShot software (HEM Data Corporation). The entire signal acquisition and amplification process was tested to be fast enough to support a chopper frequency of up to 2.5 kHz [2,13]. Signal chopping is used to help differentiate the signal from baseline drift and noise. The amplified, chopped signal acquired from the two detectors is processed through a fast Fourier transform (FFT) program to produce the corresponding "unchopped" time-domain signal. In order to obtain temperature values from two-color radiation data, the micropyrometer must be calibrated. A black body cavity heater was constructed [2,13]. The black body cavity was electrically heated to various known temperatures (determined by a thermocouple) and the output from the two IR detectors was recorded. The ratios of detector signal outputs (2–5.2 μm wavelength) were calibrated to the black body cavity temperatures. Fig. 3 gives

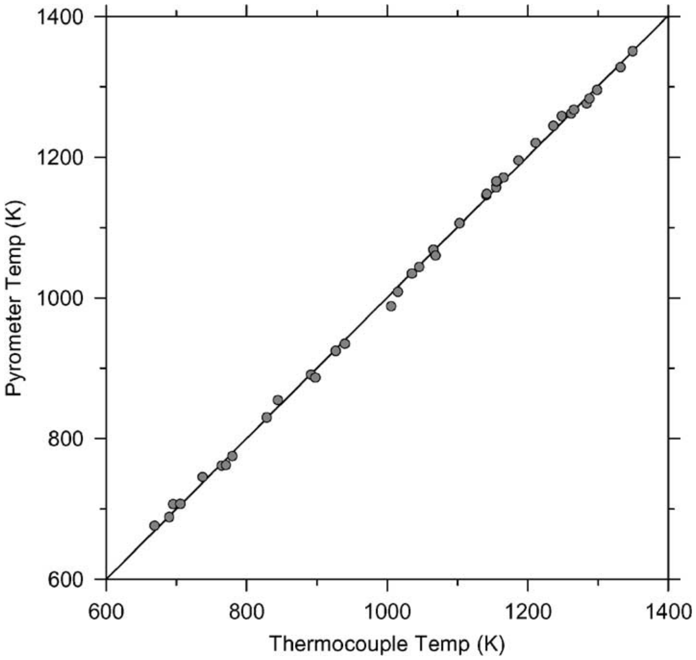

Fig. 3. The temperature calibration curve of the pyrometer.

the temperature calibration curve of the pyrometer ($r^2 = 0.999$).

A mechanical flip mirror in the optical path of the radiation is used to divert the image of the particle onto a sensitive, remote-head CCD camera (Cohu 6400 series, minimum detectable light level 0.0125 lx). This image is used to visually position the particle at the focal point of the laser.

Success of two-color micropyrometry is largely dependent on the chosen wavelengths. For a surface temperature of 500 K, the ratio of the radiation energy emitted at 2.0 μm wavelength to radiation emitted at 5.0 μm wavelength is 0.02. The same at surface temperature of 2000 K is 10.0, therefore, for a four times increase in temperature there is a 500 times increase in the detector response. This accounts for a highly sensitive detection and hence reduction in temperature measurement error. Fig. 4 shows a sensitivity analysis of errors due to non-gray effects (analysis is similar to that by Baxter et al. [14]). The emissivity ratios for the two selected wavelengths ranged from 0.6 to 1.4, where a maximum temperature error of ±450 K may exist at 2000 K. Baxter et al. suggest that the spectral emissivity for high rank coals in the size range of 40–115 μm may range from 0.7 to 0.98 and 0.5 to 0.98 for lignites. However, as the temperature is increased and devolatilization is completed, the non-gray effects from the resulting char diminish. A ventilation flow around the particle surface will also reduce the non-gray effect due to vapor cloud, therefore, a flow around the particle to remove the cloud is a must. The advantage of the two wavelengths chosen is that it provides for highly sensitive detection. At high temperature range where the non-gray effects are minimum, the accuracy of the measurement is high. However, at moderate temperatures (where devolatilization occurs), the spectral emissivity at 5.2 μm has been shown to change as a function of the extent of mass release. This may introduce errors of up to 100 K in this region as seen in Fig. 4, at 1000 K (a 10% error). Keeping in sight, the single particle nature of these experiments, the temperature variations may well exceed the 10% error limit simply because of particle to particle heterogeneity (shape and maceral composition). But in the present study, the model char system should allow for high precision in the temperature measurement because of non-devolatilizing nature and highly consistent particle properties.

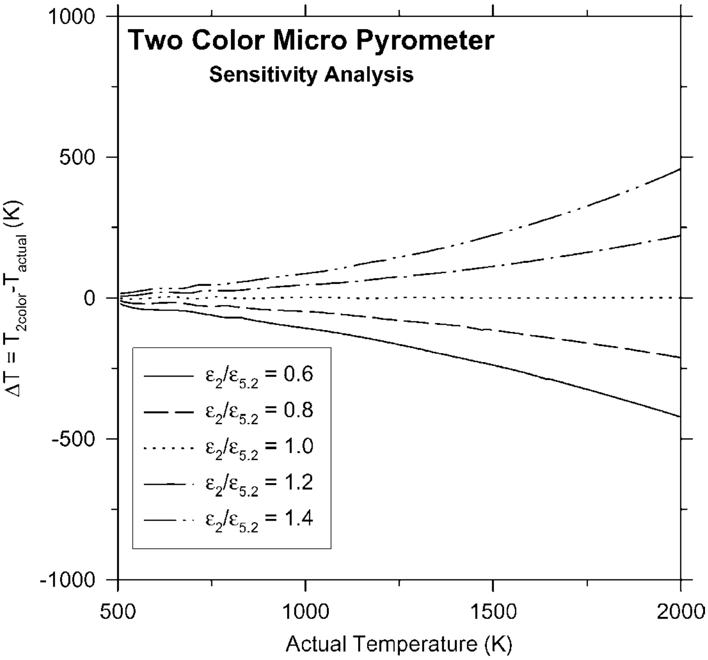

Fig. 4. Predicted errors in two-color micropyrometry temperature measurements if the emittance at 2.0 μm ($\varepsilon_{2.0}$) and 5.2 μm ($\varepsilon_{5.2}$) wavelengths were different.

2.3. Sample selection

Spherocarb particles were selected as a model char. These particles have a porosity of 0.6 (with 10% deviation) and are composed entirely of carbon [15] with only minor non-carbon impurities. This makes well documented thermophysical property data readily available. Fig. 5 shows a 120 μm Spherocarb particle placed on an electron microscopy (EM) grid with 45 μm grid spacing and 5 μm thick grid bars.

2.4. Experimental procedure

Spherocarb particles (Analabs) of approximately 80, 100 and 120 μm diameter are individually hand-picked by means of a stainless steel needle under a stereo microscope (100× magnification) and deposited on a copper EM grid. The diameter of each particle is approximately measured by visual comparison against the grid spacing (for example, the Spherocarb particle shown in Fig. 5 is approximately 120 μm in diameter). The particle on the EM grid is positioned at the center of the intersection of the two CO_2 laser beams (the center of the intersection is determined with the help of the HeNe laser guide beams). The particle is then irradiated by a 30 ms CO_2 laser pulse. Simultaneously, the surface temperature

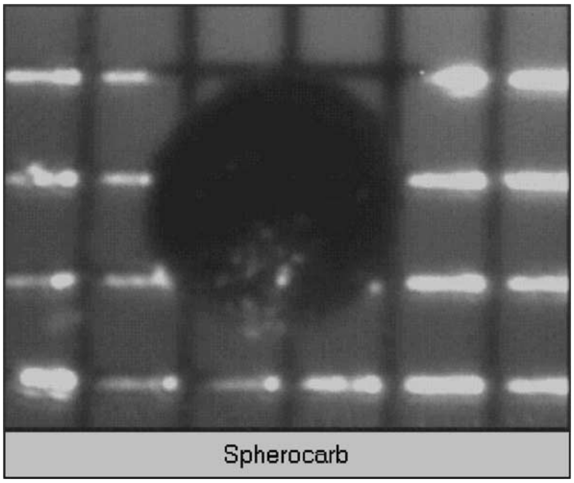

Fig. 5. Spherocarb particle (approximately 120 μm diameter) placed on a copper EM grid. The grid spacing is 50 μm.

history of the laser heated particle is measured by the two-color micropyrometer. Two different laser energy flux settings are used for each particle size. For each category (i.e. particle size/laser flux combination) at least four individual particles are irradiated to provide an estimate of statistical variability.

3. Heat transport model

The response of the two-color pyrometer is limited to radiation emitted from the particle surface, thus permitting measurement of surface temperatures. This raises two questions, "to what extent are surface temperature data useful for chemical kinetics calculations in the presence of intraparticle temperature gradients?" and "however precise the temperature measurements may be, are they real?" That is to say that these measurements need to be validated. To answer these questions, a heat transport model was developed in order to: (a) estimate intraparticle temperature gradients; (b) lend confidence to measured particle surface temperature histories.

To determine the modeling approach, a Biot number analysis is required. For a 100 μm diameter (D_p) Spherocarb particle, with thermal conductivity (K_p) of 1.25 W/(m K) [16] and at 1000 K particle temperature (ambient at 300 K), the heat transfer coefficient of convection (h) to air is 1300 W/(m^2 K) when the velocity of air is 0.25 m/s [17]. With these numbers, the Biot number ($N_{Bi} = D_p h/K_p$) is about 0.11. Since $N_{Bi} > 0.1$, lumped capacitance analysis cannot be used [18,19] (if $N_{Bi} < 0.1$, then error associated with the lumped capacitance method is small [19]) because the resistance to heat transport inside the particle is greater than that outside the particle.

3.1. Model assumptions

To reduce the complexity of the modeling problem, four simplifying assumptions are made, as described in the following paragraphs.

Assumption 1. All particles are perfectly smooth and spherical in shape.

This assumption allows the use of spherical coordinates and also permits the generation of easily defined boundary conditions [5–7].

Assumption 2. Particles are non-porous and non-reacting.

It is assumed that there is no material exchange between the particle and the surrounding atmosphere. This assumption reduces a possible heat and mass transfer problem into just a heat transfer problem [5–7].

Assumption 3. The laser beams irradiate the particle from all sides.

This assumption eliminates the spatial gradients. However, the total laser flux needs to be corrected so as to achieve the best fit. A direct method of measuring laser power absorbed by the particle is not available. Hence, absorbed laser power is used as a fitting parameter. A similar procedure was followed by Monazam and Maloney [6], where the absorbtivity of the particle was used as a fitting parameter.

Assumption 4. Thermal conductivity and specific heat capacity is calculated using Merrick's model.

Specific heat capacity is calculated by using Merrick's model [20] with the assumption that Spherocarb is entirely made up of carbon. The thermal conductivity of Spherocarb is calculated by Merrick's formula for coal char thermal conductivity [16]. Fig. 6 shows a visual representation of the assumptions and comparison to reality.

3.2. Heat transport model equations

Based upon the above assumptions, the heat transport problem can be divided into six simple steps.

Statement (a). The laser beam is the only source of energy for the particle.

The energy flux (Q_{in}) is supplied homogeneously to the entire particle surface,

$$Q_{in} = I_0 a \tag{1}$$

where I_0 is the incident laser flux and a is the absorbtivity.

Statement (b). There are two pathways for energy dissipation fluxes (Q_{out}) from the particle, namely, convection ($Q_{convection}$) and radiation ($Q_{radiation}$).

The conduction losses from the particle surface to the EM grid are assumed to be negligible because the

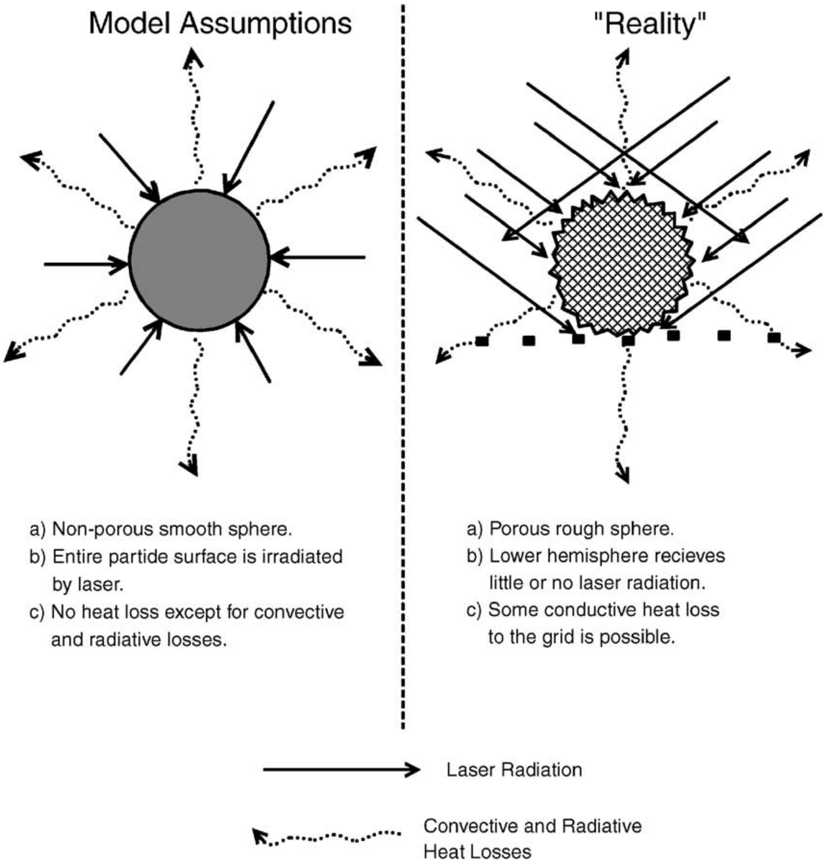

Fig. 6. Visual representation of model assumptions and comparison to reality.

area of contact of particle and EM grid is negligible. Both convection and radiation losses are equally distributed over the entire particle surface. Therefore,

$$Q_{\text{convection}} = h(T_s - T_a) \tag{2}$$

where h is the convection heat transfer coefficient, T_s is the particle surface temperature and T_a is ambient temperature. Furthermore,

$$Q_{\text{radiation}} = \sigma\varepsilon(T_s^4 - T_a^4) \tag{3}$$

where σ is the Stefan–Boltzman Constant and ε is the emissivity, assumed to be 0.8 [7]. Therefore,

$$Q_{\text{out}} = h(T_s - T_a) + \sigma\varepsilon(T_s^4 - T_a^4) \tag{4}$$

where Q_{out} is the total heat loss flux.

Statement (c). The difference between the energy fluxes, described in Eqs. (1) and (4) is the amount of energy transferred by conduction within the particle.

In other words, the net energy uptake equals laser energy absorbed minus the total heat loss by radiation and convection. Mathematically,

$$K_c \left(\frac{\partial T}{\partial r}\right)_{\text{at}\, r=R} = I_0 a - \{h(T_s - T_a) + \sigma\varepsilon(T_s^4 - T_a^4)\} \tag{5}$$

where K_c is the particle thermal conductivity and r is the radial position inside the particle of radius R and T is the temperature at radial position r and time t.

Eq. (5) becomes a boundary condition at the surface of the particle, i.e. Eq. (5) holds true at the surface of the particle.

To determine the heat transfer coefficient, h, we use the approach outlined by Bird et al. [17]. First the

Nusselt number (N_{Nu}) is calculated from which the heat transfer coefficient can be determined.

For natural convection (stationary atmosphere around the particle),

$$N_{\mathrm{Nu}} = 2 + 0.6(N_{\mathrm{Gr}})^{1/4}(N_{\mathrm{Pr}})^{1/3} \tag{6a}$$

where N_{Gr} $(=2D_{\mathrm{p}}^{3}\rho_{\mathrm{g}}g(T_{\mathrm{s}}+T_{\mathrm{a}})/(T_{\mathrm{s}}-T_{\mathrm{a}})/\mu_{\mathrm{g}}^{2})$ is the Grashoff Number and N_{Pr} $(=C_{\mathrm{g}}\mu_{\mathrm{g}}/K_{\mathrm{g}})$ is Prandtl Number and g is the acceleration due to gravity, ρ_{g}, C_{g}, μ_{g} and K_{g} the density, specific heat capacity, viscosity and thermal conductivity of the surrounding gas, respectively and D_{p} is the particle diameter. The thermophysical properties of surrounding gas are calculated at the boundary layer film temperature $(=(T_{\mathrm{s}}+T_{\mathrm{a}})/2)$.

For forced convection (gas flow around the particle),

$$N_{\mathrm{Nu}} = 2 + 0.6(N_{\mathrm{Re}})^{1/2}(N_{\mathrm{Pr}})^{1/3} \tag{6b}$$

where N_{Re} $(=D_{\mathrm{p}}^{3}\rho_{\mathrm{g}}v/\mu_{\mathrm{g}})$ is Reynolds Number and v is the velocity of the surrounding gas.

$$h = \frac{N_{\mathrm{Nu}}K_{\mathrm{g}}}{D_{\mathrm{p}}} \tag{7}$$

Thermophysical properties of the surrounding gas (here, air) are available [21,22].

Eq. (6b) is used to calculate the convective heat transfer coefficient, due to the presence of flow around the particle.

Statement (d). At the center of the particle the temperature gradient is zero due to the symmetry.

That is,

$$\left(\frac{\partial T}{\partial r}\right)_{r=0} = 0 \tag{8}$$

Eq. (8) is the boundary condition at $r = 0$.

Statement (e). Before the laser is fired, the particle is assumed to be at thermal equilibrium with the surrounding atmosphere.

That is,

$$T = T_{\mathrm{a}} \tag{9}$$

Statement (f). A finite element energy balance gives the governing equation.

$$\rho_{\mathrm{c}}C_{\mathrm{c}}\frac{\partial T}{\partial t} = \frac{1}{r^{2}\partial(r^{2}K_{\mathrm{c}}\partial T/\partial r)/\partial r} \tag{10}$$

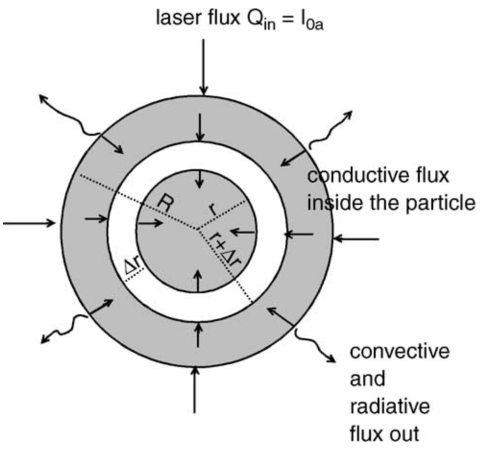

Fig. 7. Graphic representation of the finite element analysis approach for a spherical particle. Arrows indicate the direction of heat flow.

where ρ_{c} is the density and C_{c} is the specific heat capacity of the particle.

Eq. (10) is the governing partial differential equation. Fig. 7 depicts the graphical representation of the finite element analysis. The thermophysical properties of the Spherocarb particle and surrounding gas are estimated by the equations shown in Table 1. Eq. (10) is solved numerically by using the ‘‘center in space and center in time (CSCT)’’ Crank–Nicholson scheme [7], where the boundary conditions are described by Eqs. (5) and (8) and the initial conditions by Eq. (9).

Table 1
Thermophysical properties of air and Spherocarb

For air [21,22]
$C_{\mathrm{g}}(T) = 1792(T+61.372)(T+674)/[T(T+1791.4)]$
$K_{\mathrm{g}}(T) = 4.48\times10^{-3}T^{-1/2}(T+662.8)/(T+2469.3)$
$\mu_{\mathrm{g}}(T) = 1.512\times10^{-6}T^{1.5}/(T+133)$
$\rho_{\mathrm{g}}(T) = \rho_{0}(T_{0}/T) = 353/T$ (ideal gas law)

For Spherocarb char [7,16,20]
$C_{\mathrm{c}}(T) = C_{0}[G(\theta_{1}/T) + 2G(\theta_{2}/T)]$,
where $G(\theta) = \theta^{2}\mathrm{e}^{\theta}/(\mathrm{e}^{\theta}-1)^{2}$, $\theta_{1}= 380$, $\theta_{2}= 1800$,
$C_{0} = R/12 = (8.314\times100)/12 = 693$
$K_{\mathrm{c}}(T) = 0.03171T^{1/2}$
$\rho_{\mathrm{c}}= 1000$
$\varepsilon = 0.8$

All properties are in SI system units.

4. Results and discussion

In modeling the temperature histories, there are two unknowns, namely: (a) total laser power absorbed by the particle; (b) the density of the Spherocarb particles.

4.1. Absorbed laser power

As mentioned earlier, a direct method for measuring the total laser power absorbed by the particle is unavailable. Therefore, total laser power absorbed is used as a fitting parameter. This is accomplished by estimating the absorbed laser power that would predict the steady state temperature reached by the particle. Steady state temperature is defined as the temperature reached by the particle when irradiated by the laser for infinite duration. This temperature is estimated by visual extrapolation of the measured temperature histories to a steady state temperature.

4.2. Apparent particle density

There are inconsistencies in the apparent density of Spherocarb particles reported by various researchers. Sarofim and co-workers [8] used 700 kg/m^3, Fletcher [3] used 900 kg/m^3 and Maloney and co-workers [5–7] used 1050 kg/m^3 and (in later work) 950 ± 80 kg/m^3 [23]. Based on the porosity of Spherocarb and the solid density of graphitic carbon [15] the apparent particle density can be estimated to be between 700 and 1000 kg/m^3 (free fall density 700 kg/m^3). Density measurements performed by D'Amore et al. [24], using an electrodynamic balance, show a Spherocarb density of 700 ± 250 kg/m^3. Density calculation by estimating the packing volume of a known amount of Spherocarb [25] gives a lower (limiting) value of 800 kg/m^3 (based on smooth, spherical, uniform sized particles assumption). Density was also determined by a "counting and weighing" technique, 0.92 mg of a $120 + 140$ mesh fraction (140 mesh has 106 μm opening and 120 mesh has 124 μm opening) of Spherocarb particles was weighed and the particles manually counted (908 particles). The density obtained from this method is 1275 ± 275 kg/m^3. The cause of variations between our measured density and those cited in the literature could be many, including unknown errors in our density measurements and presence of absorbed species (moisture, CO_2 and other gases) in Spherocarb. However, for heat transport modeling, best empirical fit is obtained with an apparent density value of 1000 kg/m^3. A sensitivity analysis on density will be discussed in following paragraphs.

4.3. Spherocarb particle surface temperature history measurements and predictions

Three diameter sizes, namely 80, 100 and 120 μm diameter Spherocarb particles were irradiated individually by a 30 ms laser pulse at two different laser power setting (estimated flux delivered at the particle are 10 MW/m^2 (low power) and 12.7 MW/m^2 (high power), respectively, for the two power settings). Four to six single particles were analyzed for each laser power setting and particle size case. The particle surface temperature histories were measured. Using the total laser flux absorbed by the particles as a fit parameter, the surface temperature history predictions were obtained. Fig. 8 depicts the surface temperature histories of 80, 100 and 120 μm diameter Spherocarb particles irradiated at two laser power settings and the corresponding model predictions. Note that the model satisfactorily predicts the heat-up profile, as well as the cool-down rates for the first 3–4 ms after beginning of cool-down. However, the later part of the cool-down profile is predicted to be slower than observed. This discrepancy will be discussed in following paragraphs. Also note that the error band of the measured temperature histories is 100 K. Figs. 9 and 10 show the predicted surface specific heat capacity and thermal conductivity histories. Table 2 lists the fixed parameters for the laser power flux, the density value for the three particle sizes and the two power settings.

4.4. Intraparticle gradient

After modeling the particle surface temperature, the same parameters are used to estimate the intraparticle temperature gradients. The predicted gradients are graphically represented in Figs. 11 and 12 as the difference between the surface temperature and various radial temperatures, at different points in time and for lower as well as higher laser power settings. The gradient maximizes within 5 ms after the start of laser radiation and from then on diminishes. Bulk average

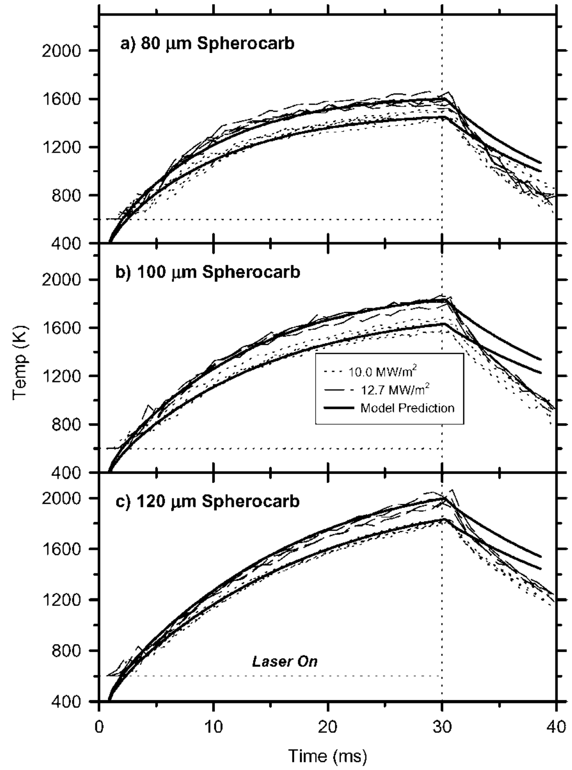

Fig. 8. Measured and predicted surface temperature histories of 80, 100 and 120 μm diameter Spherocarb particles irradiated at two different CO_2 laser power flux settings.

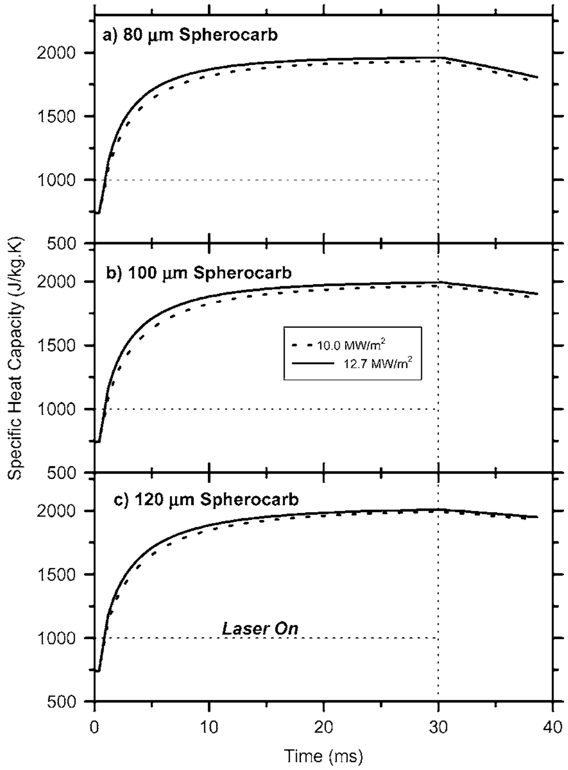

Fig. 9. Predicted particle surface specific heat capacity histories of 80, 100 and 120 μm diameter Spherocarb particles for two laser power flux settings.

radial position is at two-thirds the radius from the center of the particle sphere. For 80 μm Spherocarb particles, at high laser power, the maximum predicted difference between bulk average temperature and surface temperature is approximately 45 K, whereas, for 100 and 120 μm Spherocarb particles this differences increase to 70 and 100 K, respectively. These differences do not exceed the 100 K error band in two-color pyrometry measurement. Little is to be gained by using non-measurable average temperatures rather than measurable surface temperature for kinetic rate and yield calculations.

Table 2
Pertinent modeling information

	80 μm Spherocarb		100 μm Spherocarb		120 μm Spherocarb	
	Low power	High power	Low power	High power	Low power	High power
Number of particles irradiated	6	5	4	4	4	4
Laser flux (MW/m^2) absorbed by the particle (model)	2.04	2.55	2.40	3.00	2.83	3.54
Laser flux (MW/m^2) delivered at the particle	10.0	12.7	10.0	12.7	10.0	12.7
Ratio of low power to high power fluxes (model)	0.8	0.8	0.8	0.8	0.8	0.8
Ratio of low power to high power fluxes (delivered at the particle)	0.79	0.79	0.79	0.79	0.79	0.79
Error bar at final temperature (K) (observed)	100	100	100	100	100	200
Density (kg /m^3) (model)	1000	1000	1000	1000	1000	1000

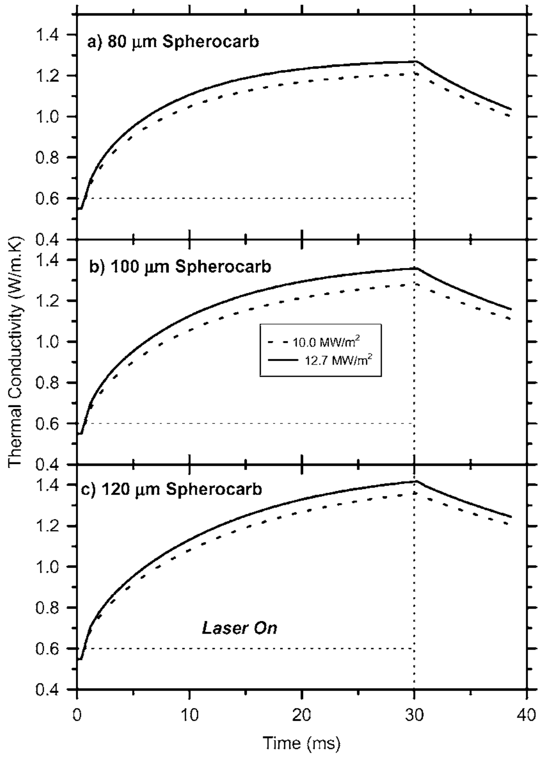

Fig. 10. Predicted particle surface thermal conductivity histories of 80, 100 and 120 μm diameter Spherocarb particles for two laser power flux settings.

4.5. Discrepancy in predicting cool-down rates

In Fig. 8, it can be observed that the model consistently predicts slower cool-down rates than observed. The potential causes of this discrepancy could be many. Two of the most likely causes will be discussed briefly. First of all, the physical property values of Spherocarb (density, specific heat capacity and thermal conductivity) used are based on estimates. Except for density, physical property values are the same as commonly used in the literature. The actual density value could well be different than that used by the model. However, in that case the model would fail to predict the heat-up rate with the current set of assumptions. Effects of a physical properties on the modeling predictions will be discussed in subsequent paragraphs. Secondly, one or more of the assumptions could be inadequate. The assumption that the laser irradiates the particle equally from all sides is used to simplify the problem to a two-dimensional problem (time and radius). However, as depicted in Fig. 6, in reality the laser beams irradiate approximately 40–60% of the particle surface and the remainder is "shadowed". This results in the non-heated part of the particle behaving as a potential heat sink, thus cooling the particle surface faster than predicted. Moreover, particle surface edge reflection and/or

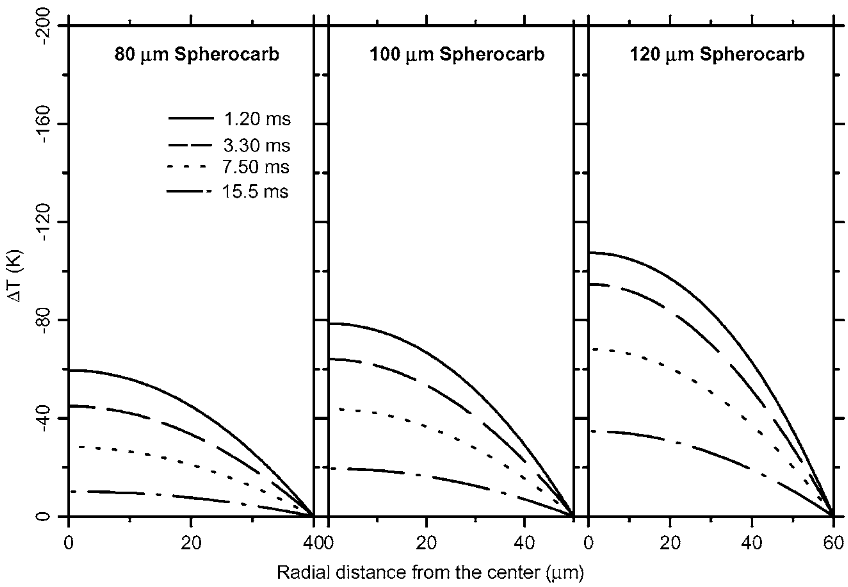

Fig. 11. Predicted temperature gradients in Spherocarb particles for 10.0 MW/m^2 laser energy flux setting ($\Delta T = T_{\mathrm{surface}} - T_{\mathrm{radial}}$).

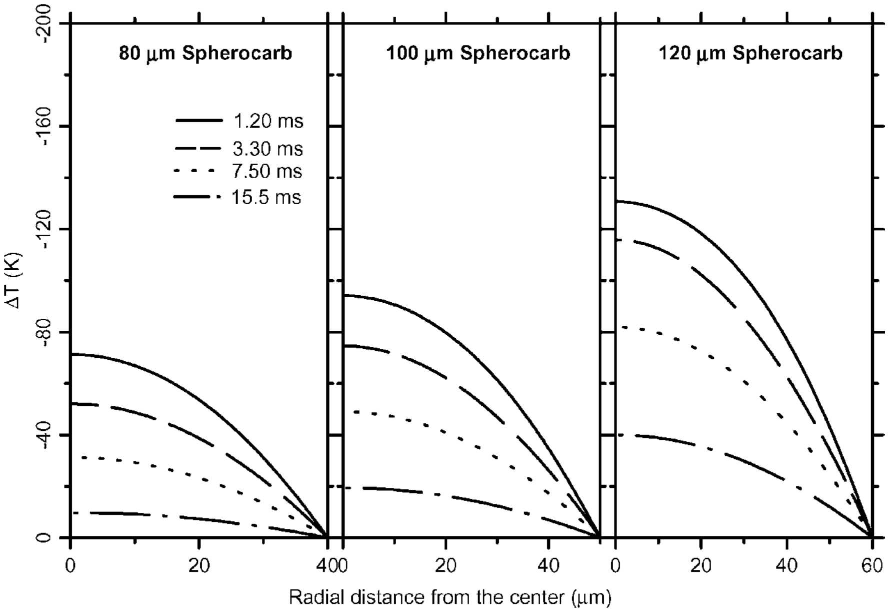

Fig. 12. Predicted temperature gradients in Spherocarb particles for 12.7 MW/m^2 laser energy flux setting ($\Delta T = T_{\text{surface}} - T_{\text{radial}}$).

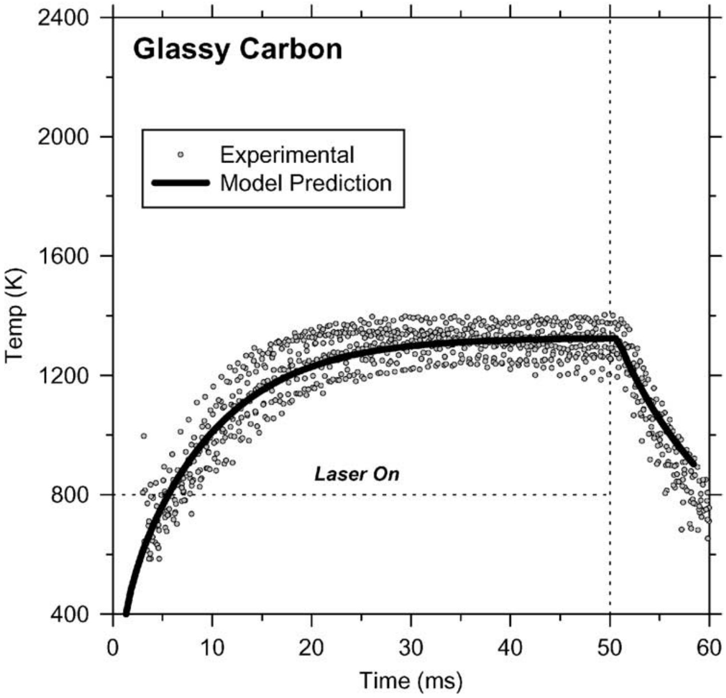

Fig. 13. Measured and predicted temperature histories of 80 μm "glassy carbon" particles irradiated with 50 ms laser pulse. Notice that the cool-down rates are well predicted by model for these non-porous particles.

fringe scattering may further reduce the amount of laser energy absorbed (because of the fact that the particle sizes are only an order in magnitude larger than the wavelength of the CO_2 laser beam) by reducing the laser absorptivity. This effect is magnified as the particle size reduces. Also, the assumptions that the particle is non-porous and smooth are not true for Spherocarb, which is rough and highly porous. To test the combined effects of porosity and smoothness we obtained non-porous "glassy carbon" particles (Alfa AESAR, stk # 38014, lot # D07D22, type 2). This batch contained 80 μm or smaller size particles. In a related set of experiments, these particle were irradiated with 50 ms laser pulses at maximum laser power output (the particles have higher reflectance than Spherocarb). The temperature histories were measured and modeled assuming the density to be 1100 kg/m^3 (at the manufacturer suggested density of 1460 kg/m^3, the model fails to predicted the observed temperature history) and 1.82 MW/m^2 (compared to 2.55 MW/m^2 for the same size Spherocarb particles) to be the total laser flux absorbed by the particles. Fig. 13 shows 14 particle surface temperature histories and the result of model prediction. Notice that both heat-up and cool-down rates are now well predicted by the model. This indicates that porosity and/or smoothness related factors may well be responsible for the observed discrepancies in cool-down rate prediction. The possible reason why porosity may not be a factor in the heat-up phase could be related to the rates of

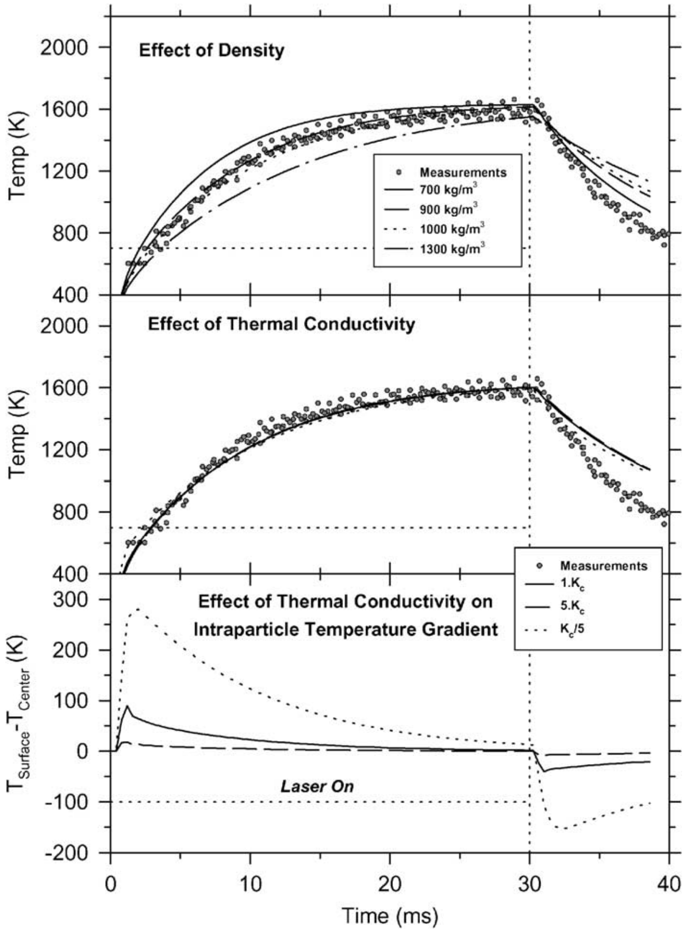

Fig. 14. Effect of change in density and thermal conductivity on temperature predictions and comparison with measured surface temperature histories of 80 μm Spherocarb particle irradiated with 30 ms 12.7 MW/m^2 laser pulse.

heat-up compared to cool-down (it is observed that heat-up rates are about half in magnitude to that of the cool-down rates).

4.6. *Effect of thermophysical properties on the model prediction*

The governing equation (Eq. (10)) incorporates thermophysical property dependencies. It is, therefore, imperative to investigate the effect of thermophysical property changes on temperature history predictions. Since specific heat capacity and density of the particle appear as multipliers ("appear together") in Eq. (10), the specific heat capacity dependency is not attempted (in order to avoid redundancy). Fig. 14 shows the effect of changes in density and thermal conductivity on temperature prediction and comparison to the measured surface temperature histories of 80 μm diameter Spherocarb particle exposed to 12.7 MW/m^2 ("high laser power") laser power flux. It is observed that as the particle density is increased the particle tends to heat-up slower and also cool-down slower. Higher density means heavier particle and hence longer response time to temperature change. A similar effect would result from increase in specific heat capacity values. The figure shows that 1000 kg/m^3 density provides the most favorable temperature prediction. It is also observed that the particle surface temperature history prediction remains unaffected by large variation in thermal conductivities (a factor of 25 change in K_c). This is due to the thermal equilibrium between the energy input and output at the surface of the particle (as described by Eq. (5)). In the case of low thermal conductivity value this results in a relatively higher temperature at the surface of the particle during the first 5 ms of the heat-up because the reduced thermal conductivity is countered by increased temperature gradients, which results in higher surface temperatures. A 25 times change in thermal conductivity reveals up to two times change in surface temperature, making the surface temperatures less sensitive to changes in thermal conductivity. But the decrease in thermal conductivity will result in large intraparticle temperature gradients. Fig. 14 shows that a gradient of up to 250 K could exist due to low values of thermal conductivity (which is realistically too low for carbonaceous solids). These gradients (predicted from low thermal conductivity values) are significant for chemical kinetics analysis and therefore, in chemical kinetics analysis thermal conductivity values must be rigorously considered.

5. Conclusions

Spherical char particles make useful model particles for testing the performance of the two-color micropyrometer for rapidly heating carbonaceous particles in the 80–120 μm size range. As particle size increases, final temperatures achieved with a given laser flux also increase along with the heating rates. This may be the summed effect of two underlying trends, namely: (a) the larger the particle size, the lower the heat transfer coefficient for convection heat loss; (b) the smaller the particle size, the stronger the laser scattering, due to wavelength effects of the CO$_2$ laser ($\lambda = 10.8$ μm). The model satisfactorily predicts the observed heat-up rates for Spherocarb particles, while under-predicting the cool-down rates. However, for non-porous "glassy carbon" type carbonaceous particles both heat-up and cool-down rates are well predicted. For the particle sizes and laser power levels used in our experiments, predicted intraparticle gradients between surface temperature and bulk average radius temperature fall within the estimated errors range of the two-color pyrometry measurements and thus can be ignored for most applications.

References

[1] W.M. Maswadeh, N.S. Arnold, W.H. McClennen, A. Tripathi, J. DuBow, H.L.C. Meuzelaar, Energy and Fuels 10 (1993) 1006–1012.
[2] W. Maswadeh, A. Tripathi, N.S. Arnold, J. DuBow, H.L.C. Meuzelaar, J. Anal. Appl. Pyrolysis 28 (1994) 55–70.
[3] T.H. Fletcher, Combustion Sci. Technol. 63 (1989) 89–105.
[4] D.J. Maloney, R.G. Jenkins, in: Proceedings of the 20th International Symposium on Combustion, The Combustion Institute, Pittsburgh, 1984, pp. 1435–1443.
[5] D.J. Maloney, E.R. Monazam, S.D. Woodraff, L.D. Lawson, Combustion Flame 84 (1991) 210–220.
[6] E.R. Monazam, D.J. Maloney, J. Appl. Phys. 71 (6) (1992) 2552–2559.
[7] E.R. Monazam, D.J. Maloney, L.O. Lawson, Rev. Sci. Instrum. 60 (11) (1989) 3460–3465.
[8] M. D'Amore, L. Tognotti, A.F. Sarofim, Combustion Flame 95 (4) (1993) 374–382.

[9] M.K. Misra, R.H. Essenhigh, Energy Fuels 2 (1988) 371–385.
[10] J.T. Yang, G.G. Wang, J. Heat Transfer 112 (1990) 192–200.
[11] G.M. Simmons, M. Gentry, J. Anal. Appl. Pyrolysis 10 (1986) 117–127.
[12] J.C. Chen, M. Taniguchi, K. Narato, K. Ito, Combustion Flame 97 (1994) 107–117.
[13] W.M. Maswadeh, Devolatilization Studies Single Coal Particles at High Heating Rates, Ph.D. Thesis, University of Utah, 4 (1996) 64–84.
[14] L.L. Baxter, T.H. Fletcher, D.K. Ottesen, Energy Fuels 2 (1988) 423–430.
[15] Analabs Chromatography Chemicals and Accessories Catalogue # K-23B, 1987, pp. 84–87.
[16] D. Merrick, Fuel 62 (1983) 553–561.
[17] R.D. Bird, W.E. Stewart, E.N. Lightfoot, Transport Phenomena, Wiley, New York, 1960.
[18] F.P. Incropera, D.P. Dewitt, Fundamentals of Heat and Mass Transfer, 3rd Edition, Wiley, New York, 1990.
[19] J.P. Holman, Heat Transfer, 6th Edition, McGraw-Hill, New York, 1986, pp. 134–135.
[20] D. Merrick, Fuel 62 (1983) 540–546.
[21] W.M. Keys, M.E. Crawford, Convection Heat and Mass Transfer, 2nd Edition, McGraw-Hill, New York, 1980.
[22] L.C. Burmeister, Convection Heat Transfer, Wiley, New York, 1983.
[23] E.R. Monazam, D.J. Maloney, in: Proceedings of the 25th International Symposium on Combustion, The Combustion Institute, Pittsburgh, 1994.
[24] A. D'Amore, R.D. Dudek, A.F. Sarofim, J.P. Longwell, Powder Technol. 56 (1988) 129–134.
[25] Perry's Chemical Engineer's Handbook, 6th Edition, McGraw-Hill, New York, 1984.